Laboratory earthquakes triggered during eclogitization of lawsonite-bearing blueschist

Sarah Incel, Nadège Hilairet, Loïc Labrousse, Timm John, Damien Deldicque, Thomas P. Ferrand, Yanbin Wang, Jörg Renner, Luiz Morales, Alexandre Schubnel

Accepted Manuscript

Laboratory earthquakes triggered during eclogitization of lawsonite-bearing blueschist

Sarah Incel, Nadège Hilairet, Loïc Labrousse, Timm John, Damien Deldicque et al.

PII: S0012-821X(16)30681-1
DOI: http://dx.doi.org/10.1016/j.epsl.2016.11.047
Reference: EPSL 14211

To appear in: *Earth and Planetary Science Letters*

Received date: 2 August 2016
Revised date: 17 November 2016
Accepted date: 24 November 2016

Please cite this article in press as: Incel, S., et al. Laboratory earthquakes triggered during eclogitization of lawsonite-bearing blueschist. *Earth Planet. Sci. Lett.* (2016), http://dx.doi.org/10.1016/j.epsl.2016.11.047

Highlights

- Brittle failure during the transition from Lws-blueschist to Lws-eclogite.
- Grain-size reduction is proposed to cause brittle failure at HP/LT conditions.
- Fast shear fuses the rock to produce lab-equivalents to natural pseudotachylites.

Laboratory earthquakes triggered during eclogitization of lawsonite-bearing blueschist

Sarah Incel[1], Nadège Hilairet[2], Loïc Labrousse[3], Timm John[4], Damien Deldicque[1], Thomas Ferrand[1], Yanbin Wang[5], Jörg Renner[6], Luiz Morales[7], Alexandre Schubnel[1]

[1] Laboratoire de Géologie de l'ENS -PSL Research University - UMR8538 du CNRS, 24 Rue Lhomond, 75005 Paris, France

[2] CNRS - UMET, Université Lille 1, 59655 Villeneuve d'Ascq, France

[3] Université Pierre et Marie Curie, 4 place Jussieu, 75252 Paris, France

[4] Freie Universität Berlin, Malteserstr. 74-100, 12249 Berlin, Germany

[5] GeoSoilEnviroCARS, University of Chicago, Argonne, IL 60439, USA

[6] Ruhr-Universität Bochum, Universitätsstraße 150, 44801 Bochum, Germany

[7] ScopeM - ETH Zürich. Auguste-Piccard-Hof 1, HPT D9, 8093, Zürich, Switzerland

Corresponding author: incel@geologie.ens.fr

Abstract

The origin of intermediate-depth seismicity has been debated for decades. A substantial fraction of these events occurs within the upper plane of Wadati-Benioff double seismic zones believed to represent subducting oceanic crust. We deformed natural lawsonite-rich blueschist samples under eclogite-facies conditions ($1.5 < P < 3.5$ GPa; $583\ K < T < 1121\ K$), using a D-DIA apparatus installed at a synchrotron beamline continuously monitoring stress, strain, phase changes, and acoustic emissions (AEs). Two distinct paths were investigated: i) heating during deformation at pressures > 2.5 GPa to maximum temperatures ranging from 762-1073 K, during which lawsonite and glaucophane became gradually unstable while entering the stability field of lawsonite-eclogite and the breakdown reaction of lawsonite was only crossed in case of the highest final temperature; ii) heating while deforming at a pressure < 2 GPa to a

maximum temperature of 1121 K associated with crossing the breakdown reaction of lawsonite and successively entering the stability fields of epidote-blueschist and eclogite-amphibolite but not of lawsonite-eclogite. Upon entering the Lws-Ecl stability field samples exhibited brittle failure, accompanied by the radiation of AEs. In-situ X-ray diffraction and microstructural analysis demonstrate that fractures are topologically related to the formation of omphacite. Amorphous material was detected along the fractures by transmission-electron microscopy without evidence for free-water. Since the newly formed omphacite crystals are small compared to the initial grains, we interpret the observed mechanical instability as a transformation-induced runaway under stress triggered during the transition from lawsonite-blueschist to lawsonite-eclogite. In contrast, we find no microstructural evidence that the breakdown of lawsonite, and hence the liberation of water leads to the fracturing in samples that experienced the highest quench temperatures of 1073 and 1121 K, although some AEs were detected during an experiment performed at 1.5 GPa. Our experimental results challenge the concept of “dehydration embrittlement”, which ascribes the genesis of intermediate-depth earthquakes to the breakdown of hydrous phases in the subducting oceanic plate. Instead we suggest that grain-size reduction (transformational faulting) during the transition from lawsonite-blueschist to lawsonite-eclogite leads to brittle failure of the deviatorically loaded samples.

Keywords: Intermediate-depth seismicity, eclogitization, transformational faulting, shear heating, dehydration embrittlement, lawsonite-blueschist

1. Introduction

Intermediate-depth earthquakes occur between approximately 50 to 300 km (Gutenberg and Richter, 1945; Hacker et al., 2003). Almost all intermediate-depth earthquakes occur in subduction zones and follow two distinct planes – the so-called upper and lower Wadati-Benioff planes of seismicity (Frohlich, 1989; Brudzinski et al., 2007). The upper plane is believed to correspond to earthquakes generated within the subducting oceanic crust while

50 the lower plane is ascribed to earthquakes located in the subjacent mantle (Hacker et al.,
51 2003).

52 For several decades, scientists have been puzzled by the occurrence of earthquakes
53 at intermediate-depths at which rocks are expected to deform plastically under the prevailing
54 pressures and temperatures (Raleigh and Paterson, 1965; Green and Burnley, 1989). A
55 multitude of theoretical, experimental, and field studies addressed this problem (e.g., Kirby,
56 1987; Green and Burnley, 1989; Hirth and Tullis, 1994; Dobson et al., 2002; Austrheim and
57 Andersen, 2004 ; Jung et al., 2004; Hacker et al., 2003; John and Schenk, 2006; Kelemen and
58 Hirth, 2007; John et al., 2009; Gasc et al., 2011; Schubnel et al., 2013; Deseta et al., 2014;
59 Thielmann et al., 2015). From these, three main hypotheses for the mechanisms of
60 intermediate-depth earthquakes emerged: i) thermal runaway or shear heating (Hobbs and
61 Ord, 1988; John et al., 2009; Prieto et al., 2013), ii) dehydration embrittlement (Green and
62 Houston, 1995; Hacker et al., 2003; Jung et al., 2004), and iii) transformational faulting (Kirby,
63 1987; Green and Burnley, 1989; Schubnel et al., 2013). The term thermal runaway describes
64 the feedback between shear heating and the temperature-dependent rock rheology. The
65 dehydration embrittlement model postulates a change from ductile to brittle behavior due to an
66 increase in pore-fluid pressure and hence a decrease in effective stress during the breakdown
67 of hydrous phases in the rock. Finally, transformational faulting refers to mechanical
68 weakening of the rock caused by volume and/or enthalpy changes but also by grain-size
69 reduction during transformation.

70 So far, most experimental work testing these hypotheses focused on serpentine-
71 dehydration experiments in the pressure-temperature range of intermediate-depth seismicity.
72 Investigating metamorphic reactions within metabasalts of the descending oceanic crust has
73 been almost completely disregarded (except for Okazaki and Hirth, 2016), although the
74 distribution of hypocenters within the subducting oceanic crust correlates very well with the
75 thermodynamically expected stability fields of different paragenesis for basaltic rock
76 compositions at elevated pressures and temperatures (Peacock and Wang, 1999; Hacker et

al., 2003; Kita et al., 2006). Indeed, hypocenter locations in cold subducting oceanic crust such as below northern Japan (Kita et al., 2006) coincide with the predicted stability field of lawsonite-eclogite (Lws-Ecl), i.e. an intermediate facies between lawsonite blueschists (Lws-Bs), comprising glaucophane and lawsonite as hydrous phases, and eclogites (Ecl) whose paragenesis of garnet + omphacite is nominally dry. The lack of seismicity once entering the stability field of eclogite is striking (Kita et al., 2006) and this seismic boundary suggests that metamorphic reactions during the transition from Lws-Bs to Ecl transiently change the rheology of the rock and enable brittle failure.

The key objective of the present contribution is to distinguish the mechanical impacts of glaucophane and lawsonite breakdown and their potential link with brittle failure. We performed deformation experiments with in-situ monitoring of phase content and acoustic emissions on lawsonite-bearing blueschist samples. The discussion focuses on the influence of metamorphic reactions during deformation on the micro- and nanostructures as well as on the record of acoustic emissions. Finally, we present a plausible mechanism for brittle failure of the samples during their transformation to eclogite.

2. The Corsican blueschist

2.1 Sample description

A lawsonite-blueschist (Lws-Bs) from Alpine Corsica served as sample material. Having experienced peak metamorphic conditions of approx. 520 ± 20 °C and 2.3 ± 0.1 GPa (Vitale Brovarone et al., 2011) it mostly consists of glaucophane (Gln, mineral abbreviations follow Whitney and Evans, 2010) and lawsonite (Lws), where Lws often appears as lenses. The Gln:Lws ratio of approx. 3:2 is estimated from optical analyses of several thin sections. The minor phases actinolite (Act), garnet (Grt), phengite (Ph), titanite (Ttn), and omphacite (Omp1), with Xjd ≈ 0.4 and Xdi ≈ 0.6, comprise less than 15 % of the rock's volume. Apatite (Ap), and albite (Ab) are also found in limited amounts (Vitale Brovarone et al., 2011). The

mineral phases Gln, Omp1, and Act were chemically investigated (Figure 1) and our analyses are in good agreement with those previously reported (Vitale Brovarone et al., 2011).

2.2 Sample preparation

A fragment of the Lws-Bs, selected for its homogeneous distribution of Gln and Lws content, was crushed, ground and sieved to a grain size fraction < 38 µm. A Frantz isodynamic magnetic separator was used to segregate Gln and Lws. Three different powders with different Gln:Lws ratios were produced: i) bulk-rock, ii) glaucophane-rich (Gln-rich), and iii) lawsonite-rich (Lws-rich) (Figure 1). Powders were used rather than the intact rock, because of i) the heterogeneity in mineralogy (e.g. due to Lws lenses) and texture (schistosity), which would considerably hamper the sample-to-sample comparison and ii) the need of a small grain-size (< 38 µm) for the in-situ X-ray powder diffraction (XRD) during the deformation of the samples (more details in 3.4).

2.3 Characterization of the starting material

Powders were embedded in epoxy and afterwards characterized by element mapping of Ca and Na using a scanning electron microscope (SEM). Element ratios were calculated using the software ImageJ (Abramoff et al., 2004) and can be directly transformed to different Gln:Lws ratios (Figure 1). The bulk-rock, Gln-rich, and Lws-rich powders show Gln:Lws ratios of approx. 1:1, 2:1, and 1:3, respectively. As in the natural rock, minor and accessory phases comprise around 15 % of the powder volume. For these three different powders, three different P-T pseudosections were calculated in the NCFMASH system using the thermodynamic modeling software Theriak-Domino (De Capitani and Petrakakis, 2010). As expected for a divariant reaction, the position of the Gln-out reaction depends on the system's stoichiometry, hence on the Gln:Lws ratio (Figure 2). The slightly lower stability of amphibole (Amp) or rather Gln at HP/ LT of the Gln-rich powder relative to the bulk-rock powder (Figure 2) is related to an increase of Fe and Mg content with increasing Gln in the system stabilizing the almandine

component of Grt. The univariant Lws-breakdown curve (Lws = Ep) shifts with bulk chemistry due to the Ca balance between garnet (grossular component) and lawsonite. The calculated stability fields of the different metabasalts and the positions of the different Gln- and Lws-out curves for the three powders (Figure 2) are in agreement with previous findings (Vitale Brovarone et al., 2011).

3. Experimental methods

3.1 Experimental setup

Deformation experiments were performed using a deformation diamond-anvil (D-DIA) apparatus, attached to the GSECARS synchrotron beamline 13-BM-D at the Advanced Photon Source Chicago. During nominal isotropic pressurization, a main ram controls the advancement of four horizontal and two vertical anvils that compress the sample assembly until a prescribed load is reached. Differential rams, which move the vertical anvils independently, create a deviatoric stress field in the sample assembly (Wang et al., 2003). Anvils are made of tungsten carbide (WC), except for two horizontal anvils composed of sintered diamond, translucent to X-rays. The use of synchrotron X-rays allows for in-situ monitoring of strain, using radiographs of the sample, but also for recording powder diffraction patterns from which phase changes and stress state are deduced. Temperature is inferred from temperature-output power calibrations with an uncertainty below 10 %. Raterron et al. 2013 demonstrated the existence of non-negligible axial temperature gradients of about 155 K/mm with the sample's center colder than the edges.

3.2 Sample assembly

The powder was placed in a cylindrical BN sleeve surrounded by the graphite furnace and placed into 9 x 9 x 8 mm amorphous Boron-epoxy cuboids. The sample is sandwiched between two gold foils and two alumina pistons (Figure 3). The initial size of the powder charge is approx. 2.1 mm in diameter by 3 mm in height. All powders were hot-isostatically pressed

before triaxial deformation at temperatures of about 583 to 653 K for approx. 1 h (Table 1). Sample BS_3_1073 was hot-pressed in a piston-cylinder apparatus at 3 GPa and 923 K for 1 day, then machined and loaded in the deformation cell assembly. This sample was kept at isostatic conditions at 583 K in the D-DIA for only 30 min.

3.3 Experimental procedure

After the hot-pressing, deformation with a strain rate of about 10^{-5} s^{-1} was started. Syndeformational heating was performed by increasing the power in steps of 10 W corresponding to a temperature increase of approx. 50 K. The heating steps were initiated at 10, 15, 20, 25, 30, and 35 % strain for the Gln-enriched and the Lws-enriched samples, at 10, 20, 30, and 40 % strain for the run BS_1.5_1121, and at 5, 12, 18, 20, 25, 30, and 35 % strain for the run BS_3_1073.

3.4 In situ data acquisition setup, stress and strain computations

The X-ray transmission images and diffraction patterns of the samples were acquired using a monochromatic synchrotron X-ray beam at 13-BMD (λ = 0.2431 Å, approx. 51 keV) during the course of deformation runs (Figure 3). The typical acquisition time for images was 2 s and for the diffraction patterns 300 s. In image mode, the beam is typically 2 mm x 3 mm, i.e., comparable to initial sample size, and the CCD camera is positioned to capture the radiograph. In diffraction mode, the CCD camera is moved out of the diffraction path and slits reduce the beam size to typically 200 x 200 microns. Therefore, only a limited volume in the center of the sample is probed. The detector tilt and rotation relative to the incident beam were calibrated using the diffraction pattern of a CeO_2 standard and the software Fit2D (Hammersley et al., 1996).

The d-spacing of a crystal is sensitive to the orientation of the diffracting plane with respect to an anisotropic stress field. For instance, the d-spacing of lattice planes oriented perpendicular to the direction of the maximum principal stress σ_1 decreases and thus the

diffraction line shifts to higher 2θ angles. Therefore, in a powder with random crystal orientations, the different responses of lattice planes to anisotropic stress result in a distortion or pseudo-ellipticity of the Debye rings that are initially circular under hydrostatic conditions. This distortion is called lattice strain and can be used as a proxy for the differential stress effectively acting on the polycrystalline aggregate (Uchida et al., 1996, Singh et al., 1998). The deviation of the diffracting plane from the normal to the maximum compression axis is characterized by an angle ψ related to the diffraction angle θ according to:

$$\cos\psi = \cos\theta\cos\delta \quad (1)$$

where δ represents the projection of ψ on the detector plane. Calculation of differential stress was performed using Fit2D (Hammersley et al., 1996) and the multifit-polydefix software (Merkel and Hilairet, 2015). The relation between the d-spacing $d_{(hkl)}$ (for a lattice plane with indices hkl) and the lattice strain $Q_{(hkl)}$ reads:

$$\frac{d_{(hkl)}(\psi) - d_{P,(hkl)}(\psi)}{d_{P,(hkl)}(\psi)} = Q_{(hkl)}\left(1 - 3\cos^2\psi\right) \quad (2)$$

(Uchida et al., 1996; Singh et al., 1998) where $d_{P,(hkl)}$ denotes the d-spacing at "hydrostatic" or isotropic stress and $d_{(hkl)}(\psi)$ corresponds to the d-spacing of the plane hkl with angle ψ to the maximum principal stress. For each experiment, the d-spacings were extracted from the diffraction patterns and fitted in a $d_{(hkl)}$ over ψ plot.

The refinement of the lattice strain relied on the $d_{P,(hkl)}$ of up to 5 crystallographic planes. The planes (110), (-111), and (151) of glaucophane were always used but sometimes also the (-202) and the (240) planes for the processing of experiments on the bulk-rock or the Gln-rich powders. For tests on the Lws-rich powder, the 3 crystallographic planes (002), (201), and (202) of lawsonite sufficed to refine the unit cell volume. We employed the second-order equation of state for Gln and Lws (Comodi et al., 1991; Mao et al., 2007) and constraints on their thermal expansion (Holland et al., 1996; Jenkins and Corona, 2006).

202 Mean stress σ_m calculates as:

203 $$\sigma_m = \frac{\sigma_1 + \sigma_2 + \sigma_3}{3} \quad (4)$$

204 where σ_1 denotes the maximum principal stress, and σ_2 and σ_3 are considered identical to the
205 confining pressure P_c determined based on the shift in peak position before and after
206 compression and heating. Differential stress $t_{(hkl)}$ was calculated for a specific plane using the
207 lattice strain $Q_{(hkl)}$ according to (2) and the effective moduli $G_{(hkl)}$:

208 $$t_{(hkl)} = 6\, Q_{(hkl)} G_{(hkl)}. \quad (3)$$

209 The effective moduli $G_{(hkl)}$ derive from the elastic compliances S_{ij} (inverted from the stiffness
210 matrix C_{ij}) for Gln (Bezacier et al., 2010) and Lws (Mao et al., 2007). In the following, the
211 differential stress is obtained by averaging the $t_{(hkl)}$ values observed for the two most intense
212 diffraction peaks. For the bulk-rock and the Gln-rich experiments, these corresponded to the
213 (110) and (151) planes of glaucophane and to the (002) and (201) planes of lawsonite for the
214 Lws-rich experiment.

215 The calculated differential stresses do not represent absolute values (see Hilairet et al.,
216 2012, for a detailed discussion). Due to difficulties in calculating the effective moduli for low-
217 symmetry phases like Gln, the calculation relied on orthorhombic instead of monoclinic
218 symmetry. For a single experiment, it was possible to simultaneously calculate the differential
219 stresses from Gln and Lws crystals. While the calculated differential stresses lie in the same
220 order for the two phases, Lws appears to support more differential stress than Gln (Figure 4c),
221 in agreement with previous experimental studies on blueschist rheology (Kim et al., 2013).

222 The powder-diffraction patterns were also used to continuously monitor the phase
223 assemblage, using diffraction peak heights for individual phases integrated over the 360° of
224 the Debye rings. While this is a crude estimate and does not take into account the effects of
225 evolution in preferred orientations, the changes in intensities observed here are consistent with
226 the microstructural observations and with the calculated pseudosections.

227 Bulk axial strain was determined using the radiographs of the samples. The gold foils
228 on top and below a sample act as strain markers due to their high X-ray absorption contrast
229 compared to the sample and the ceramic pistons. The current length of the sample was
230 determined by measuring the distance between the shadows of the gold foils and strain ε was
231 calculated by comparing the change in sample length, ΔL, the initial length L before the
232 deformation was started, i.e.:

233 $$\varepsilon = \frac{\Delta L}{L} \quad (5)$$

234 Strain rate was calculated by relating the strain to the time increments between radiographs.

235 **3.5 Acoustic emission setup and localization technique**

236 Piezoceramic lead-zirconate transducers with a thickness of 0.5 mm, a diameter of 10
237 mm, and a resonance frequency of 2-4 MHz (see also Schubnel et al., 2013, for details of the
238 setup) were placed behind each of the six anvils (Figure 3). Acoustic emission (AE) waveforms
239 were acquired simultaneously from all six transducers by a multi-channel oscilloscope.
240 Emissions were recorded over the entire duration of each experiment, including cold
241 compression, hydrostatic heating, deformation, and syndeformational heating sequence, then
242 quenching and decompression. In fact, during the first stage of compression many AEs were
243 recorded, which are attributed to powder compaction. From ca. 1 GPa to the final confining
244 pressure (Table 1), no further AEs were recorded demonstrating that the AEs subsequently
245 recorded during triaxial deformation are not caused by the compaction. Furthermore, previous
246 deformation experiments with the same acoustic setup and the same sample assembly (Gasc
247 et al., 2011) demonstrated that except for the porous alumina, deformation of the cell materials
248 does not result in AEs, thus excluding the assembly as a cause for the AEs recorded in the
249 present study.

250 Locations of AEs were determined using a constant P-wave velocity of 8000 m/s
251 determined by previous experiments with the same experimental setup (Schubnel et al., 2013).

It is assumed that the travel time within each anvil remains constant over the course of an experiment. The travel time in the sintered diamond anvils was calculated to be 0.78 µs lower than in the WC anvils. Picking of the first arrivals was performed manually as the total number of AEs recorded during deformation was limited. The travel time was first corrected for anvil type, then the difference in arrival times between each pair of facing anvils was interpreted as a difference in travel-time within the sample assembly. The precision of the location of AEs along each of the three axis between the 3 anvil pairs lies within the sensor thickness of around 0.5 mm. The exact localization of each hypocenter in the sample would require a more sophisticated AE data analysis which lies beyond the scope of the present study.

4. Results

Our study comprises six deformation experiments using the three powders at the experimental conditions shown in Table 1. The sample nomenclature uses letters to represent the powder type, i.e. BS for blueschist bulk-rock, GLN for Gln-rich, and LWS for the Lws-rich powder, and numbers to give confining pressure in GPa and the quench temperature in K on the second and third position, respectively.

4.1 Mechanical Data, in-situ XRD analysis, and AE records

Differential stress decreased during syndeformational heating in all tests, i.e., independent of sample composition (Figure 4a-f). The recorded diffraction patterns reveal that the intensity of the Omp (-221) peak, the most intense peak of Omp, first increases above approx. 573 K but decreases above 700 K all the way to the end of the deformation (Figure 4g- i). The sample, which was hot-pressed in a piston-cylinder, initially shows more Omp, but follows the same Omp (-221) intensity evolution as the other samples hot-pressed in the D-DIA (Figure 4i). The Lws (002) peak completely disappears in bulk-rock samples (BS_1.5_1121, BS_3_1073) passing 734 and 1020 K, respectively (Figure 4d, j, f, l). The intensity of this peak decreases but does not vanish for samples enriched with either Lws

(LWS_2.5_925) or Gln (GLN_2.5_927) quenched at around 830 K. The intensity remains constant in the lowest temperature experiment, quenched at 762 K well before the breakdown of Lws (GLN_2.5_762, Figure 4e, k).

Acoustic emissions tend to occur in two clusters – one at low temperatures (around 640 to 700 K) and one at higher temperatures (approx. 830 to 1121 K) (Figure 4m-o), but not every experiment actually yield both clusters. For example, the experiment on a sample with bulk-rock composition (BS_1.5_1121) conducted at the lowest confining pressure of 1.5 GPa exhibits only the high-temperature cluster (Figure 4m), while a sample with the same composition deformed at a confining pressure of approx. 3 GPa only shows the low-temperature cluster (Figure 4o).

4.2 Microstructural Analyses – SEM and EMPA

Observed microstructures are similar for the suite of experiments. Only the bulk-rock sample deformed at the lowest confining pressure of 1.5 GPa (BS_1.5_1121) exhibits no fracture related to deformation (Figure 5g). We focus here on presenting four representative experiments, one representing each powder composition and additionally the low-pressure bulk-rock experiment (BS_1.5_1121), which shows no macroscopic strain localization. The microstructure of the sample quenched at the lowest temperature (GLN_2.5_762) is shown in the supplementary material in Figure S1. The Gln-enriched sample (GLN_2.5_927) and the Lws-enriched sample (LWS_2.5_925) were both deformed at a confining pressure of approx. 2.5 GPa (Table 1) and quenched before the complete breakdown of Lws expected from the computed pseudosection (Figure 2). The tests on the bulk-rock powder (BS_1.5_1121, BS_3_1073) were performed at 1.5 and 3 GPa, respectively, and quenched after the breakdown of Lws.

4.2.1 Microstructural and chemical analysis of the Gln-enriched sample

The Gln-enriched sample (GLN_2.5_927) exhibits two fractures starting in the lower corners of the sample extending diagonally towards the sample center (Figure 5a). Several

303 narrow fractures, oriented parallel to the main fractures, dissect and offset grains of Lws and
304 Omp1 (Figure 5b). The horizontal fracture is a typical decompression feature.

305 A narrow fracture parallel to a main fracture shows slightly brighter than average edges
306 in backscattered electron (BSE) mode, indicating a change in chemistry (Figure 5c). Profiles
307 across such a fracture show Ca enrichment in the brighter zones at the fracture edges (Figure
308 6b, d) related to the formation of a second generation of omphacite. In comparison to Omp1
309 of the starting material, this secondary omphacite, called Omp2 in the following, has a higher
310 jadeite component of $X_{jd} \approx 0.7$. Mineral chemical data (wavelength-dispersive (WDX) and
311 energy-dispersive X-ray spectrometry (EDX)) of Omp2 of all samples after deformation was
312 plotted in a Ca-Al-Na ternary plot to demonstrate chemical variations of Omp2 (open circles in
313 Figure 6c) and for the main phases Gln, Omp1, and Act of the natural blueschist (solid circles
314 in Figure 6c). Strikingly, the composition of Omp2 plots between the Gln and Omp1
315 composition of the natural Lws-Bs (Figure 6c). These microstructural observations match well
316 with the growth of the Omp (-221) peak during the first stage of the deformation (Figure 4g, h,
317 i). The incipient breakdown of Lws is evidenced by its association with small epidote (Ep)
318 needles - its dehydration product at low-pressure/high-temperature (LP/HT) conditions (Figure
319 5b).

320 *4.2.2 Microstructure and mineral chemical analysis of the Lws-enriched sample*

321 The Lws-enriched sample is cross-cut by two main fractures (Figure 5d). Several
322 narrow fractures are oriented parallel or sub-parallel to these main fractures. Along one of
323 these narrow fractures, Gln grains are observed that are dissected and offset (Figure 5e). The
324 fracture edges exhibit a brighter than average contrast, resulting from Omp2 (Figure 5f). Most
325 of the Omp2 crystals are located along fractures as was found for the Gln-enriched sample
326 (GLN_2.5_927), too.

327 In most places, the fracture-filling material was lost during preparation of the samples,
328 but some fractures are still filled by a material appearing dark in BSE mode (Figure 5e) implying
329 that its average atomic number is smaller than the adjacent Lws and Gln crystals (Figure 5e).

These zones are so narrow that EDX or WDX measurements give mixed analysis of filling material and rock matrix. After the interaction with the electron beam, this dark material always shows holes implying a poor crystallinity.

4.2.3 Microstructure and chemical analysis of the bulk-rock samples

The samples prepared from bulk-rock powder (BS_1.5_1121, BS_3_1073) were performed at two different confining pressures, 1.5 GPa and 3 GPa, and quenched after the breakdown of Lws. Pseudomorphs after Lws appear as patches filled with Ep needles (Figure 5i, k). Their occurrence is in good agreement with the thermodynamically expected stability of Lws (Figure 2). After deformation, the lowest pressure experiment (BS_1.5_1121) only shows a horizontal decompression crack, but no macroscopic strain localization (Figure 5g). Rims of Ca-Amp formed around Gln grains (Figure 5i). The high-pressure sample (BS_3_1073) is completely cross-cut by sample-size fractures (Figure 5j). Brighter zones along fractures, pores, and rims around Gln crystals were identified as Omp2 (Figure 5k, l). This sample also shows crystals offset along shear fractures (Figure 5k). Garnet grains exhibit growth zonation with Ca enrichment in the rim relative to its core (Figure 6a). A filled fracture between two Gln crystals shows tiny crystals “floating” within a dark material filling the fracture (Figure 5l) of which the larger ones, with an idiomorphic crystal shape, were classified as Omp2. Holes left after EDX and WDX measurements within this zone suggest that this dark material is poorly crystalline or amorphous. Observations on samples prepared in a piston-cylinder apparatus (as the hot-pressed sample BS_3_1073, see 3.2) show no evidence that this amorphous material represents a remnant of an incomplete reaction (supplementary material Figure S2).

4.3 Nanostructural Analysis – Transmission electron microscopy (TEM)

The focused ion beam (FIB) sections for the Gln-enriched sample (GLN_2.5_927) were cut across a fracture with edges indicating Omp2 and Ca-Amp. The TEM images taken in bright field (BF) mode document the structure of the fracture at different scales (Figure 7). The sealed fracture appears brighter in the TEM images relative to the surrounding material

356 indicating that this area is either thinner, poor in heavy atoms or less crystalline than the
357 surrounding phases. The adjacent grains were identified as Ca-Amp and Omp2 (Figure 7b).
358 The contact between the fracture filling-material and Omp2 and the absence of spots in the
359 diffraction pattern reveal that the material filling out the fracture is amorphous (Figure 7c).
360 Grains next to the fracture exhibit 120° triple junctions (Figure 7c).

361 The FIB section in the sample prepared from the bulk-rock sample (BS_3_1073) was
362 cut across a narrow, sealed fracture along which a pair of displaced garnet crystal was found.
363 The TEM images were also taken in BF mode. The most striking observation is the occurrence
364 of a bright, according to diffraction analyses amorphous material appearing as bubbles (Figure
365 8a, d) or pockets in the matrix sometimes “trapped” within nests of Ep-needles (Figure 8e).
366 These bubbles and pockets are completely absent in the Gln-enriched sample (GLN_2.5_927)
367 quenched before the Lws-breakdown. The fracture, across which this FIB section was cut,
368 appears to be filled by idiomorphic shaped garnet crystals varying in size (Figure 8f),
369 surrounded by a bright, amorphous groundmass (Figure 8c, f, g). Amorphous material thus
370 occurs at two structurally different sites, bubbles and pockets in the matrix or filling material in
371 fractures. The grains next to the fracture were in most cases found to be Omp2 (Figure 8c, d).
372 Unfortunately, it was not possible to obtain precise chemical analysis of the amorphous
373 material in either FIB section.

374 **5. Discussion**

375 **5.1 Comparison between experiments quenched before and after Lws breakdown**

376 The *P-T* path experienced by a sample during deformation controls its microstructure,
377 phase assemblage and the occurrence of AEs (Figure 9). At high P_c (> 3 GPa), experiments
378 only show an early low-temperature AE cluster at around 638–701 K. Experiments at
379 intermediate P_c (around 2.5 GPa) exhibit two successive clusters, one at low temperatures of
380 638–701 K and one at high temperatures of around 831 – 927 K. Finally, the experiment at

low P_c (< 1.5 GPa) only exhibits a high-temperature AE cluster beginning at around 873 K and not ceasing until the end of the experiment at 1121 K. Thus, the pattern of AE occurrence during syndeformational heating strongly depends on confining pressure, regardless of the powder type used for the experiment (Figure 4m, n, o).

The samples quenched after the Lws breakdown (BS_1.5_1121, BS_3_1073) differ from those quenched before (GLN_2.5_927, LWS_2.5_925) by the occurrence of pseudomorphs after Lws and bubbles composed of amorphous material interpreted as a quenched Lws-breakdown derived fluid. The appearance of Ep in the high pressure experiment (BS_3_1073) suggests either that the experiment was quenched at lower pressure than calculated, that Ep stability extends to higher pressures than thermodynamically predicted, or that it survives metastably (Figure 9). Except for the bubbles which are absent in the nanostructure of the Gln-enriched sample (GLN_2.5_927) micro- and nanostructures are similar for the Lws-enriched sample (LWS_2.5_925), the high-pressure bulk-rock sample (BS_3_1073) and the Gln-enriched sample (GLN_2.5_927). All three samples exhibit amorphous material filling fractures with adjacent Omp2 crystals (Figures 7c, 8c, d).

5.2 Transition from Lws-Bs to Lws-Ecl

Mean stress is used as a measure of thermodynamic pressure assuming that the change in slope of the equilibrium curves under non-hydrostatic conditions can be neglected (MacDonald, 1957; Kirby, 1987). During the first stage of deformation the calculated mean stress and the confining pressure differ by 0.7-1 GPa (Figure 9; Table 1). The difference decreases towards the end of the experiments due to the decrease in differential stress with increasing temperature (Figure 4a- f). The uncertainty regarding the relevant thermodynamic state variable does not affect the prognosis from the calculated *P-T* pseudosections that the experiments performed at P_c > 2.5 GPa enter the Lws-Ecl stability field except of the experiment performed at P_c < 2 GPa (Figures 2, 9).

406 The occurrence of the low-temperature AE cluster (shown as stars in Figure 9) matches
407 the expected transition conditions for Lws-Bs to Lws-Ecl and the growth of the (-221) peak of
408 omphacite (Figure 4). The powder diffraction pattern were taken from a small volume of the
409 sample center and therefore do not quantify spatial stress heterogeneities in the samples, e.g.,
410 stress concentrations at the edges, that might lead to local variations in phase stability.
411 Combined with the observation that Omp2 occurs along shear fractures, the correlation of
412 formation of Omp2 with the low-temperature AE records suggests that its appearance at HP/LT
413 triggered the brittle failure of the sample. The formation of Omp2 is related to the breakdown
414 of Gln and the liberation of Ca derived from the successive disappearance of Lws at HP (Lws-
415 Bs ≈ 19% Lws to Lws-Ecl ≈ 13% Lws, Figure 2).

416 The amorphous material filling the fractures suggests that slip along the fracture
417 generated a melt (likely due to frictional heating) out of which idiomorphic crystals grew
418 (Figures 8f, 7c). The absence of bubbles and pockets acts as evidence that the reaction
419 initiating the brittle failure of the sample released no or only minor amounts of fluid in the Gln-
420 enriched sample (GLN_2.5_927) quenched before the breakdown of Lws at HT (Figure 7).
421 Therefore, we suppose that the grain-size reduction during the formation of Omp2 at HP/LT
422 may have acted as weakening mechanism (Spray, 1995) and that nanocrystalline Omp2 at the
423 edges of the fracture may represent remnants of the nucleation zones for failure (Figure 5c, f).
424 Due to the small grain size the Omp2 crystals could only be distinguished in FIB sections at
425 the TEM and therefore a significant quantification of the grain-size distribution was not
426 possible. The notion of a rapid transformation to Omp2 is supported by the chemical and
427 structural similarity between Omp2 and Gln and the recognition that Ca diffusion, derived from
428 Lws, is fast and possibly even enhanced by a high grain-boundary density during the reaction
429 (Putnis, 2014).

430 Our observations of a high Jd content of Omp2 (X_{jd} ≈ 0.7 %) texturally linked to Gln is
431 in accord with the breakdown reaction for glaucophane, Gln → 2 Jd + Tlc, quoted by Carman
432 and Gilbert, 1983. This exothermic reaction with an enthalpy of reaction of about -8.9 kJ

433 (Holland, 1988) may facilitate the generation of a melt. However, HP talc (Tlc) was neither
434 found in the XRD nor in any of the samples after deformation in contrast to its occurrence in
435 MORB (Wei and Clarke, 2011). The absence of Tlc in our samples may result from (partial)
436 melting of the reaction products during fast shear. The amorphous material should show a
437 chemistry close to talc stoichiometry, but within this study it was not possible to precisely
438 analyze the amorphous material.

439 The sample prepared with bulk-rock composition (BS_3_1073), which entered the Lws-
440 Ecl stability field at HP/LT, showing only the low-temperature cluster of AEs is the only one
441 which exhibits newly grown Ca-rich Grt coronas (Figure 6a) and idiomorphically shaped Grt
442 crystals are "floating" within the amorphous fracture-filling materials (Figure 8). These newly
443 formed Grt crystals can be linked to the metamorphic reaction 4 Gln + 3 Lws → 8 Jd + 3 Di +
444 3 Prp + 7 Qtz + 7 H_2O (Evans, 1990). The absence of Grt in all other samples might be related
445 to a combination of its high nucleation barrier and the lack of initial Grt grains in the starting
446 material acting as nucleation sites (Rubie, 1998). In samples where Grt is absent, the
447 amorphous material filling the fractures might represent the sink for Fe and Mg liberated from
448 Gln.

449 **5.3 Breakdown of lawsonite**

450 The *P-T* domain in which the high-temperature AEs were recorded matches with the
451 thermodynamically expected breakdown of Lws (Figure 9). Therefore, we suppose that these
452 AEs were triggered by the associated dehydration reaction. The microstructure of the sample
453 deformed under the lowest confining pressure (BS_1.5_1121), that did not enter the stability
454 field of Lws-Ecl (Figure 9), reveals the absence of macroscopic strain localization (Figure 5g).
455 The recorded AEs are therefore either linked to fractures that are overprinted by ongoing
456 plastic deformation or to other processes during dehydration, e.g. the formation of
457 pseudomorphs after lawsonite or the growth of Ca-Amp rims around Gln (Figure 5h, i). The
458 observation that most of the high-temperature AEs do not coincide with bigger stress drops

and were mostly recorded while heating additionally strengthens the interpretation that these AEs were not caused by the brittle failure of the samples (Figure 9). In contrast to our observations, a recently published experimental study reported that dehydration of Lws leads to brittle fracturing accompanied by AEs (Okazaki and Hirth, 2016). Okazaki and Hirth 2016 used almost pure lawsonite samples and this difference in chemical composition of the starting material could explain the contrasting observations.

5.4 Link to natural observations

The relocalization of seismic events below Hokkaido, NE Japan, shows that they occur where the expected position of the subducting oceanic crust coincides with the upper Wadati-Benioff plane (Kita et al., 2006). Additional information from thermodynamic modeling implies a link between metamorphic reactions during the eclogitization of Lws-Bs and seismicity (Hacker et al., 2003; Kita et al., 2006). The involvement of the breakdown of hydrous phases (lawsonite and amphibole) during eclogitization leads to the proposition of dehydration embrittlement as possible mechanism for intermediate-depth seismicity (Hacker et al., 2003; Jung et al., 2004; Okazaki and Hirth, 2016). Yet, a recent study on source-parameter modelling and the energy budget of intermediate-depth earthquakes of the Bucaramanga Nest, Columbia (Prieto et al., 2013), concluded that the combination of narrow shear zones (less than 3 cm), rapid stress drops, and localized temperature increase is best explained by shear heating. A geochemical, petrological, and micro-textural study investigating the formation of pseudotachylites (PST) in metagabbros from Alpine Corsica comes to a similar conclusion (Deseta et al., 2014). The analyzed PSTs show different water contents ranging from 0–4 wt. % and the authors therefore suggest that the dehydration of hydrous phases is unlikely to trigger the formation of PST at high pressure. The authors explain the generation of melt due to fusion of the wall rock minerals. The amount of water present in the PST will therefore only depend on the availability of hydrous minerals in the fracture zone and their fusion during fast shear. Since PSTs are also be found in anhydrous rocks like lower crustal gabbros (Andersen

et al., 1990; John et al., 2009) the instability related to Lws breakdown may well result from strain localization due to aspects of the reaction other than the dehydration, e.g. density change, grain-size reduction, and liberation of heat during reaction. Numerical simulations show that grain-size reduction and shear heating are the most likely causes for the formation of HP-pseudotachylites (John et al., 2009; Thielmann et al., 2015).

6. Conclusions

We experimentally reproduced the transition from lawsonite-blueschist to lawsonite-eclogite, the expected metamorphic evolution of a lawsonite-bearing blueschist during cold subduction. We did not find any evidence for a straightforward link between the breakdown of Lws and the failure of the samples that would support a mechanism akin to dehydration embrittlement. Instead we showed that metamorphic reactions during the transition from lawsonite-blueschist to lawsonite-eclogite can cause fracturing accompanied by AEs matching observations from seismicity locations in cold subduction zones, numerical simulations, and field observations. Shear fractures are decorated with newly grown omphacite grains, enriched in Jd content and texturally linked to Gln, which suggests that the breakdown reaction for glaucophane, Gln → 2 Jd + Tlc may have played a role in triggering shear instabilities. We argue that grain-size reduction due to the formation of nanocrystalline secondary omphacite grains and latent heat release by the reaction act in conjunction as weakening mechanism triggering the brittle failure of the samples. Shear heating fuses the wall rock next to the fracture surface and the melt is later quenched as amorphous material filling the fractures – a possible laboratory equivalent to natural pseudotachylites.

Acknowledgement

The authors would like to thank Christian Chopin for providing the blueschist sample for this study. The research leading to these results has received funding from the People Program (Marie Curie Actions) of the European Union's Seventh Framework Program FP7/2017-2013/

under REA grant agreement n° 604713 and from the Agence Nationale pour la Recherche (project “DELF” ANR-12-JS06–0003). Portions of this work were performed at GeoSoilEnviroCARS (The University of Chicago, Sector 13), Advanced Photon Source (APS), Argonne National Laboratory. GeoSoilEnviroCARS is supported by the National Science Foundation - Earth Sciences (EAR-1128799) and Department of Energy- GeoSciences (DE-FG02-94ER14466). This research used resources of the Advanced Photon Source, a U.S. Department of Energy (DOE) Office of Science User Facility operated for the DOE Office of Science by Argonne National Laboratory under Contract No. DE-AC02-06CH11357.

519 Abramoff, M.D., Magalhaes, P.J., Ram, S.J., 2004. Image Processing with ImageJ.
520 Biophotonics International, 11, 7, 36-42

521 Andersen, T., Austrheim, H., Burke, E.A.J., 1990. Fluid inclusions in granulites and eclogites
522 from the Bergen Arcs, Caledonides of W. Norway. Mineral. Mag. 54, 145–158.

523 Austrheim, H., Andersen, T.B., 2004. Pseudotachylytes from Corsica: Fossil earthquakes from
524 a subduction complex. Terra Nov. 16, 193–197. doi:10.1111/j.1365-3121.2004.00551.x

525 Bezacier, L., Reynard, B., Bass, J.D., Wang, J., Mainprice, D., 2010. Elasticity of glaucophane,
526 seismic velocities and anisotropy of the subducted oceanic crust. Tectonophysics 494,
527 201–210. doi:10.1016/j.tecto.2010.09.011

528 Brudzinski, M.R., Thurber, C.H., Hacker, B.R., Engdahl, E.R., 2007. Global Prevalence of
529 Double Benioff Zones. Science (80-.). 316, 1472–1474. doi:10.1126/science.1139204

530 Carman, J.H., Gilbert, M.C., 1983. Experimental studies on glaucophane stability. Am. J. Sci.,
531 283-A, 414-437,

532 Comodi, P., Mellini, M., Ungaretti, L., Zanazzi, P.F., 1991. Compressibility and high pressure
533 structure refinement of tremolite, pargasite and glaucophane. Eur. J. Mineral. 3, 485–499.

534 De Capitani, C., Petrakakis, K., 2010. The computation of equilibrium assemblage diagrams
535 with Theriak/Domino software. Am. Mineral. 95, 1006–1016. doi:10.2138/am.2010.3354

536 Deseta, N., Ashwal, L.D., Andersen, T.B., 2014. Initiating intermediate-depth earthquakes:
537 Insights from a HP-LT ophiolite from Corsica. Lithos 206-207, 127–146.
538 doi:10.1016/j.lithos.2014.07.022

539 Dobson, D.P., Meredith, P.G., Boon, S. a., 2002. Simulation of subduction zone seismicity by
540 dehydration of serpentine. Science 298, 1407–1410. doi:10.1126/science.1075390

541 Evans, B.W., 1990. Phase relations of epidote-blueschists. Lithos 25, 3–23. doi:10.1016/0024-
542 4937(90)90003-J

543 Frohlich, C., 1989. The nature of deep-focus earthquakes. Ann. Rev. Earth Planet. Sci. 17,
544 227–254.

545 Gasc, J., Schubnel, A., Brunet, F., Guillon, S., Mueller, H.J., Lathe, C., 2011. Simultaneous
546 acoustic emissions monitoring and synchrotron X-ray diffraction at high pressure and
547 temperature: Calibration and application to serpentinite dehydration. Phys. Earth Planet.
548 Inter. 189, 121–133. doi:10.1016/j.pepi.2011.08.003

549 Green, H. and Houston, H., 1995. the Mechanics Earthquakes 169–213.

550 Green, H.W., Burnley, P., 1989. A new self-organizing mechanism for deep-focus
551 earthquakes. Nature 341, 733–737. doi:10.1038/341733a0

552 Gutenberg, B., Richter, C.F., 1945. Seismicity of the earth. Bull. Geol. Soc. Am. 56, 603–667.
553 doi:10.1130/0016-7606(1945)56[603:SOTE]2.0.CO;2

554 Hacker, B.R., Peacock, S.M., Abers, G.A., Holloway, S.D., 2003. Subduction factory 2. Are
555 intermediate-depth earthquakes in subducting slabs linked to metamorphic dehydration
556 reactions? J. Geophys. Res. 108, 2030. doi:10.1029/2001JB001129

557 Hammersley, A.P., Svensson, S.O., Hanfland, M., Fitch, A.N., Hausermann, D., 1996. Two-
558 dimensional detector software: From real detector to idealised image or two-theta scan.
559 High Press. Res. 14, 235–248. doi:10.1080/08957959608201408

560 Hilairet, N., Wang, Y., Sanehira, T., Merkel, S., Mei, S., 2012. Deformation of olivine under
561 mantle conditions: An in situ high-pressure, high-temperature study using monochromatic
562 synchrotron radiation. J. Geophys. Res. Solid Earth 117. doi:10.1029/2011JB008498

563 Hirth, G., Tullis, J., 1994. The brittle-plastic transition in experimentally deformed quartz
564 aggregates. J. Geophys. Res. 99, 11731–11747. doi:10.1029/93JB02873

565 Hobbs, B.E., Ord, A., 1988. Plastic instabilities: Implications for the origin of intermediate and
566 deep focus earthquakes. J. Geophys. Res. Solid Earth 93, 10521–10540.
567 doi:10.1029/JB093iB09p10521

568 Holland, T.J.B., 1988. New Heat Capacity and Thermodynamic Data. Cell 134–142.

569 Holland, T.J.B., Redfern, S.A.T., Pawley, A.R., 1996. Volume behavior of hydrous minerals at
570 high pressure and temperature: II. Compressibilities of lawsonite, zoisite, clinozoisite, and
571 epidote. Am. Mineral. 81, 341–348.

572 Jenkins, D.M., Corona, J.C., 2006. Molar volume and thermal expansion of glaucophane.
573 Phys. Chem. Miner. 33, 356–362. doi:10.1007/s00269-006-0083-0

574 John, T., Medvedev, S., Rüpke, L.H., Andersen, T.B., Podladchikov, Y.Y., Austrheim, H., 2009.
575 Generation of intermediate-depth earthquakes by self-localizing thermal runaway. Nat.
576 Geosci. 2, 137–140. doi:10.1038/ngeo419

577 John, T., Schenk, V., 2006. Interrelations between intermediate-depth earthquakes and fluid
578 flow within subducting oceanic plates: Constraints from eclogite facies pseudotachylytes.
579 Geology 34, 557–560. doi:10.1130/G22411.1

580 Jung, H., Green II, H.W., Dobrzhinetskaya, L.F., 2004. Intermediate-depth earthquake faulting
581 by dehydration embrittlement with negative volume change. Nature 428, 545–549.
582 doi:10.1038/nature02412

583 Kelemen, P.B., Hirth, G., 2007. A periodic shear-heating mechanism for intermediate-depth
584 earthquakes in the mantle. Nature 446, 787–790. doi:10.1038/nature05717

585 Kim, D., Katayama, I., Michibayashi, K., Tsujimori, T., 2013. Rheological contrast between
586 glaucophane and lawsonite in naturally deformed blueschist from Diablo Range,
587 California. Isl. Arc 22, 63–73. doi:10.1111/iar.12003

588 Kirby, S.H., 1987. Localized polymorphic phase transformations in high-pressure faults and
589 applications to the physical mechanism of deep earthquakes. J. Geophys. Res. 92,
590 13789. doi:10.1029/JB092iB13p13789

591 Kita, S., Okada, T., Nakajima, J., Matsuzawa, T., Hasegawa, A., 2006. Existence of a seismic
592 belt in the upper plane of the double seismic zone extending in the along-arc direction at

593 depths of 70-100 km beneath NE Japan. Geophys. Res. Lett. 33, 1–5.
594 doi:10.1029/2006GL028239

595 MacDonald, G.J.F., 1957. Thermodynamics of solids under non-hydrostatic stress with
596 geologic applications. Am. J. Sci. doi:10.2475/ajs.255.4.266

597 Mao, Z., Jiang, F., Duffy, T.S., 2007. Single-crystal elasticity of zoisite Ca2Al3Si3O12 (OH) by
598 Brillouin scattering. Am. Mineral. 92, 570–576. doi:10.2138/am.2007.2329

599 Merkel, S., Hilairet, N., 2015. *Multifit* / *Polydefix* : a framework for the analysis of polycrystal
600 deformation using X-rays. J. Appl. Crystallogr. 48, 1307–1313.
601 doi:10.1107/S1600576715010390

602 Okazaki, K., Hirth, G., 2016. Dehydration of lawsonite could directly trigger earthquakes in
603 subducting oceanic crust. Nature 530, 81–4. doi:10.1038/nature16501

604 Peacock, S.M.S., Wang, K., 1999. Seismic consequences of warm versus cool subduction
605 metamorphism: examples from southwest and northeast japan. Science 286, 937–9.
606 doi:10.1126/science.286.5441.937

607 Prieto, G.A., Florez, M., Barrett, S.A., Beroza, G.C., Pedraza, P., Blanco, J.F., Poveda, E.,
608 2013. Seismic evidence for thermal runaway during intermediate-depth earthquake
609 rupture. Geophys. Res. Lett. 40, 6064–6068. doi:10.1002/2013GL058109

610 Putnis, a., 2014. Why Mineral Interfaces Matter. Science (80-.). 343, 1441–1442.
611 doi:10.1126/science.1250884

612 Raleigh, C.B., Paterson, M.S., 1965. Experimental deformation of serpentinite and its tectonic
613 implications. J. Geophys. Res. 70, 3965. doi:10.1029/JZ070i016p03965

614 Raterron, P., Merkel, S., Holyoke, C.W., 2013. Axial temperature gradient and stress
615 measurements in the deformation-DIA cell using alumina pistons. Rev. Sci. Instrum. 84.
616 doi:10.1063/1.4801956

617 Rubie, D.C., 1998. Disequilibrium during metamorphism: the role of nucleation kinetics. What

618 Drives Metamorph. Metamorph. React. Spec. Publ. 138 138, 199–214.
619 doi:10.1144/GSL.SP.1996.138.01.12

620 Schubnel, A., Brunet, F., Hilairet, N., Gasc, J., Wang, Y., Green, H.W., 2013. Deep-focus
621 earthquake analogs recorded at high pressure and temperature in the laboratory. Science
622 341, 1377–80. doi:10.1126/science.1240206

623 Singh, A.K., Balasingh, C., Mao, H., Hemley, R.J., Shu, J., 1998. Analysis of lattice strains
624 measured under nonhydrostatic pressure. J. Appl. Phys. 83, 7567. doi:10.1063/1.367872

625 Spray, J.G., 1995. Pseudotachylyte controversy: fact or friction? Geology. doi:10.1130/0091-
626 7613(1995)023<1119:PCFOF>2.3.CO

627 Thielmann, M., Rozel, A., Kaus, B.J.P., Ricard, Y., 2015. Intermediate-depth earthquake
628 generation and shear zone formation caused by grain size reduction and shear heating.
629 Geology 43, 791–794. doi:10.1130/G36864.1

630 Uchida, T., Funamori, N., Yagi, T., 1996. Lattice strains in crystals under uniaxial stress field.
631 J. Appl. Phys. 80, 739–746. doi:10.1063/1.362920

632 Vitale Brovarone, A., Groppo, C., Hetényi, G., Compagnoni, R., Malavieille, J., 2011.
633 Coexistence of lawsonite-bearing eclogite and blueschist: Phase equilibria modelling of
634 Alpine Corsica metabasalts and petrological evolution of subducting slabs. J. Metamorph.
635 Geol. 29, 583–600. doi:10.1111/j.1525-1314.2011.00931.x

636 Wang, Y., Durham, W.B., Getting, I.C., Weidner, D.J., 2003. The deformation-DIA: A new
637 apparatus for high temperature triaxial deformation to pressures up to 15 GPa. Rev. Sci.
638 Instrum. 74, 3002–3011. doi:10.1063/1.1570948

639 Wei, C.J., Clarke, G.L., 2011. Calculated phase equilibria for MORB compositions: A
640 reappraisal of the metamorphic evolution of lawsonite eclogite. J. Metamorph. Geol. 29,
641 939–952. doi:10.1111/j.1525-1314.2011.00948.x

642 Whitney, D.L., Evans, B.W., 2010. Abbreviations for names of rock-forming minerals. Am.

643 Mineral. 95, 185–187. doi:10.2138/am.2010.3371

644

Figures

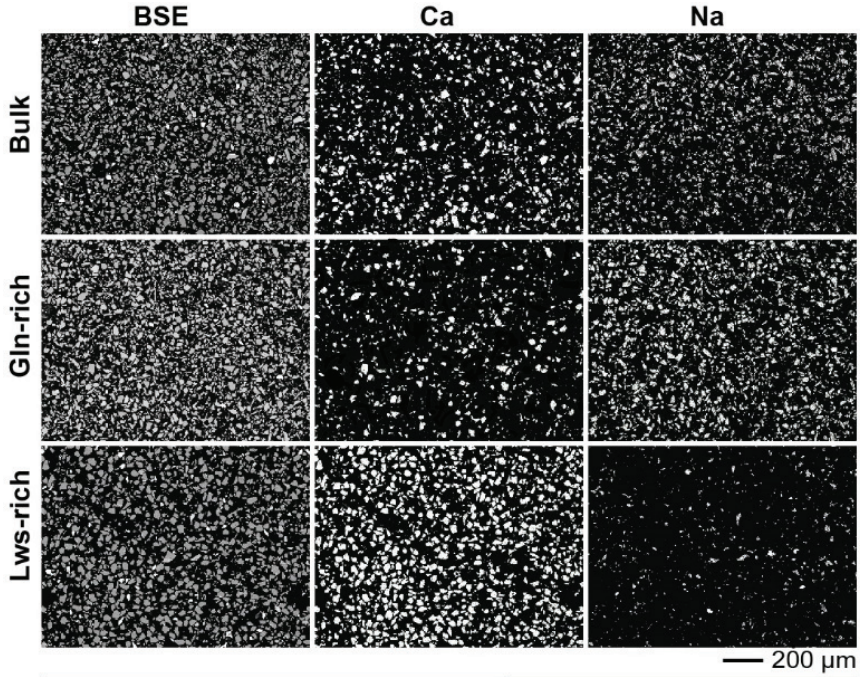

Oxides	Gln	Lws	Act	Omp1
SiO_2	58.42	38.34	58.36	56.07
Al_2O_3	10.81	32.56	0.75	8.79
CaO	0.61	17.39	11.93	13.59
Na_2O	7.39	0.00	0.58	6.70
FeO	11.27	0.34	9.37	7.13
MgO	9.69	0.00	18.08	8.01
K_2O	0.03	0.002	0.06	0.04
MnO	0.11	0.00	0.49	0.22
TiO_2	0.00	0.04	0.07	0.08
Cr_2O_3	0.03	0.02	0.00	0.00
Total	98.36	88.70	97.71	100.64

	Ca [%]	Na [%]
Bulk	46	54
Gln/ Lws ≈ 1 :1		
Gln-rich	33	67
Gln/ Lws ≈ 2 :1		
Lws-rich	71	29
Gln/ Lws ≈ 1 :3		

Figure 1: Characterization of the three different powders and their Ca:Na ratios and chemical analyses of major phases of the Corsican blueschist.

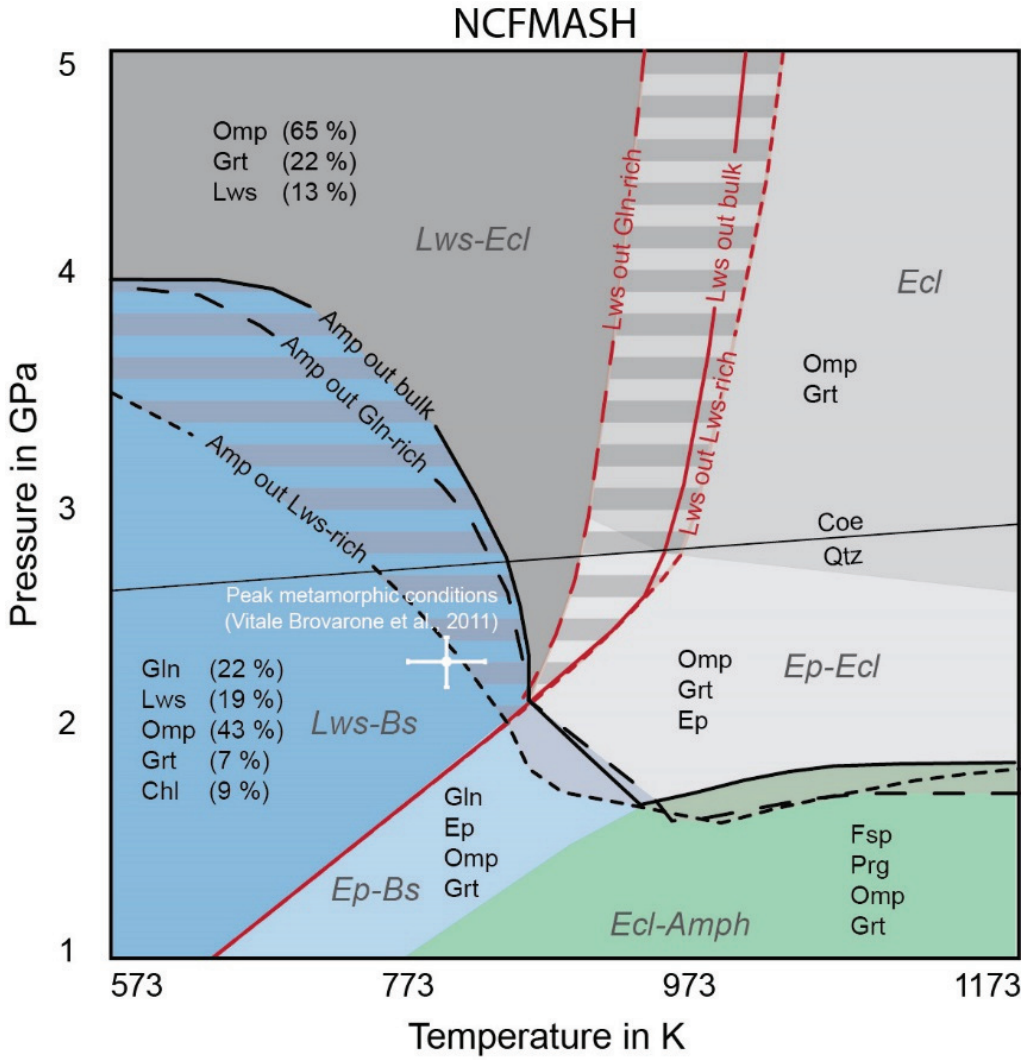

649

650 **Figure 2:** Summarized *P-T* pseudosection showing the Amp- and the Lws-out curves for the
651 three different powders (Lws-Ecl: lawsonite-eclogite, Lws-Bs: lawsonite-blueschist, Ep-Bs:
652 epidote-blueschist, Ecl-Amph: eclogite-amphibolite, Ep-Ecl: epidote-eclogite, Ecl: eclogite).

653

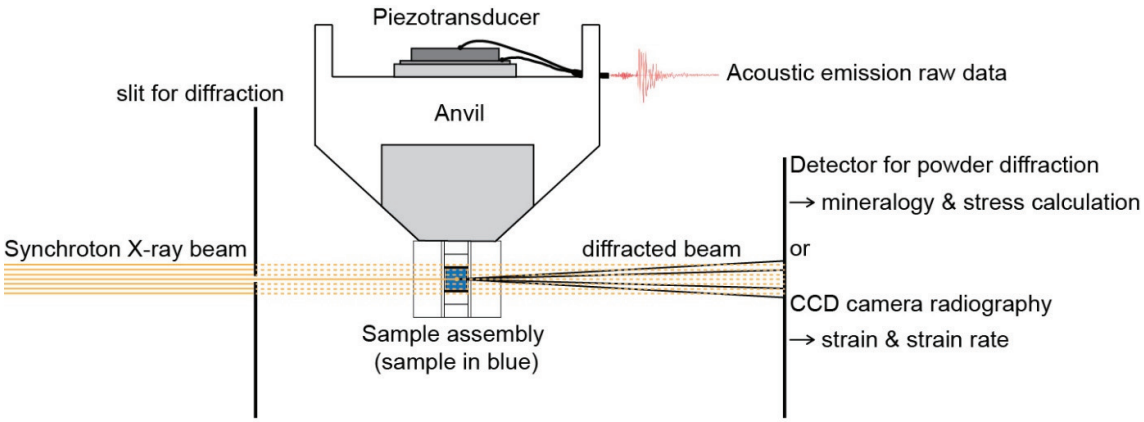

Figure 3: Schematic drawing of the experimental setup for the D-DIA experiments. For the sake of clarity only the upper vertical anvil is shown.

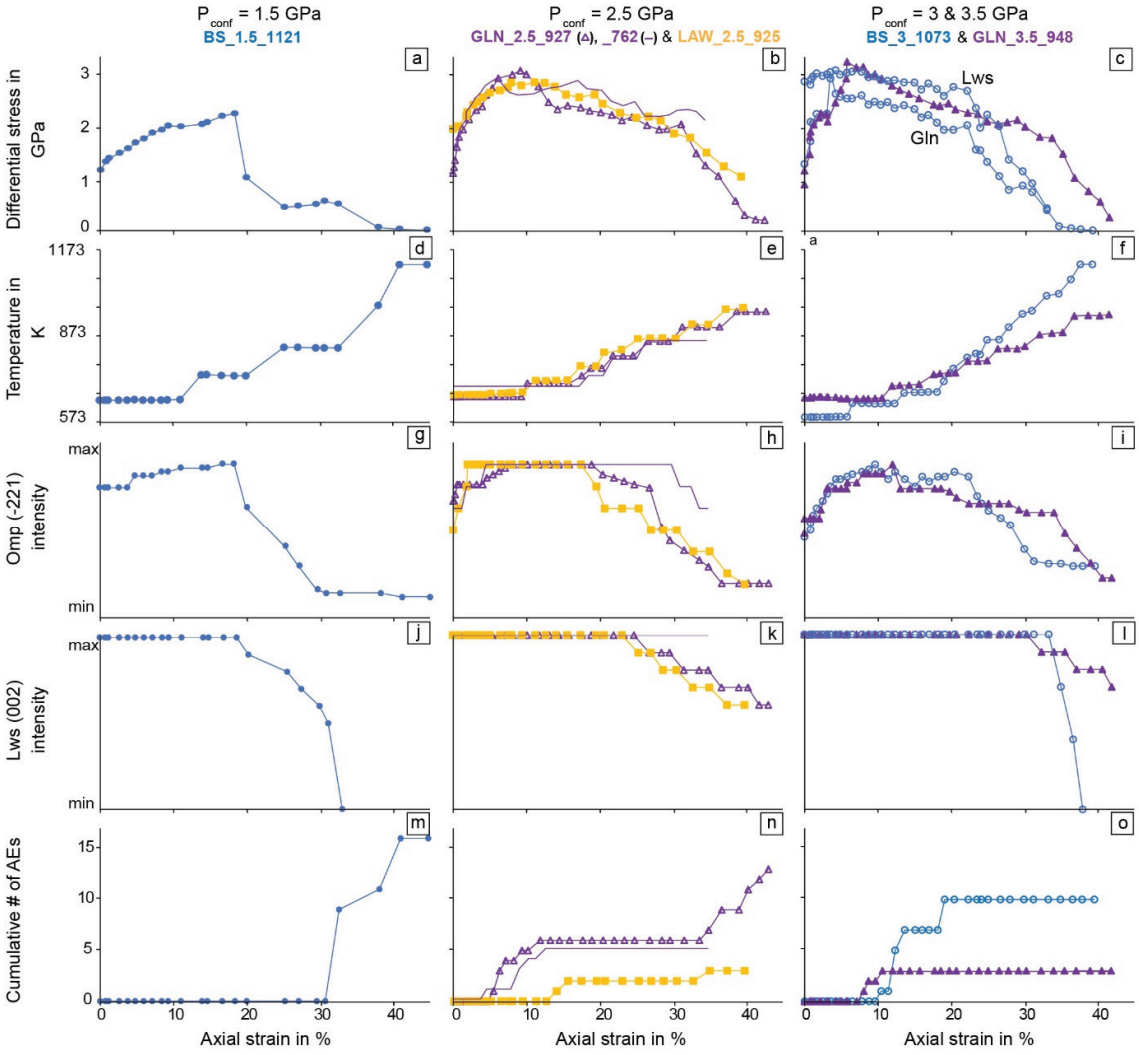

Figure 4: Mechanical data and peak intensities (proxy for phase proportion) from in-situ XRD, and record of AEs. The columns represent the low pressure (1.5 GPa), the intermediate pressure (2.5 GPa), and the high pressure (3 - 3.5 GPa) experiments (from left to right). Color code: bulk-rock in blue, Gln-rich powder in violet, Lws-rich powder in yellow. For the run BS_3_1073 it was possible to calculate the differential stress on Gln and Lws.

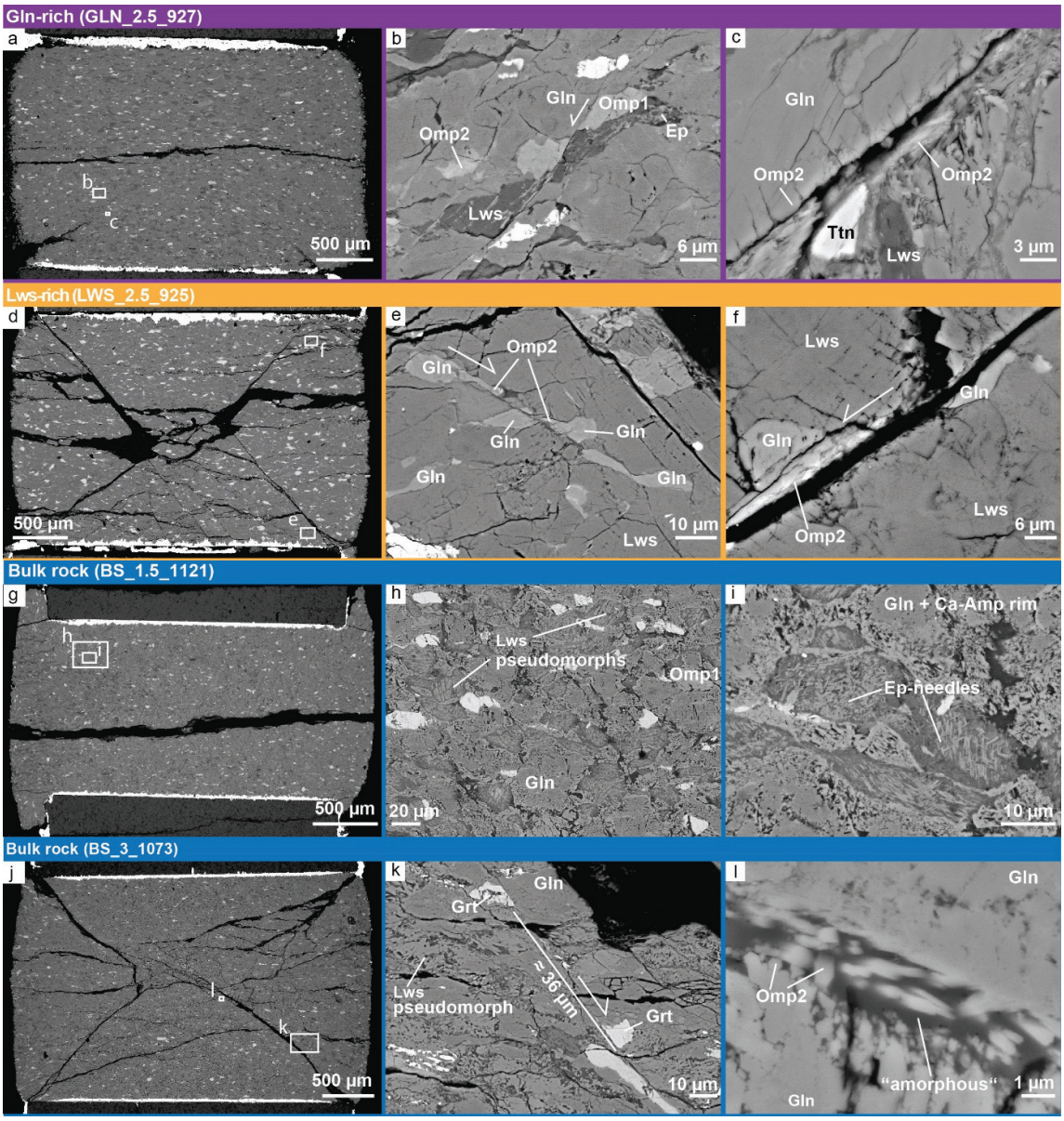

Figure 5: BSE images taken at the SEM using an acceleration voltage of 15 kV. The four rows represent the microstructure of the runs GLN_2.5_927 (a, b, c), LWS_2.5_925 (d, e, f), BS_1.5_1121 (g, h, i), and BS_3_1073 (j, k, l). The color represents the starting material used for the experiment (violet: Gln-rich, yellow: Lws-rich, and blue: bulk-rock). The BSE images a, d, g, and j are overview images of the samples GLN_2.5_927, LWS_2.5_925, BS_1.5_1121, and BS_3_1073, respectively, after deformation. The maximum compression direction σ_1 is oriented vertically on the images (parallel to the short edge).

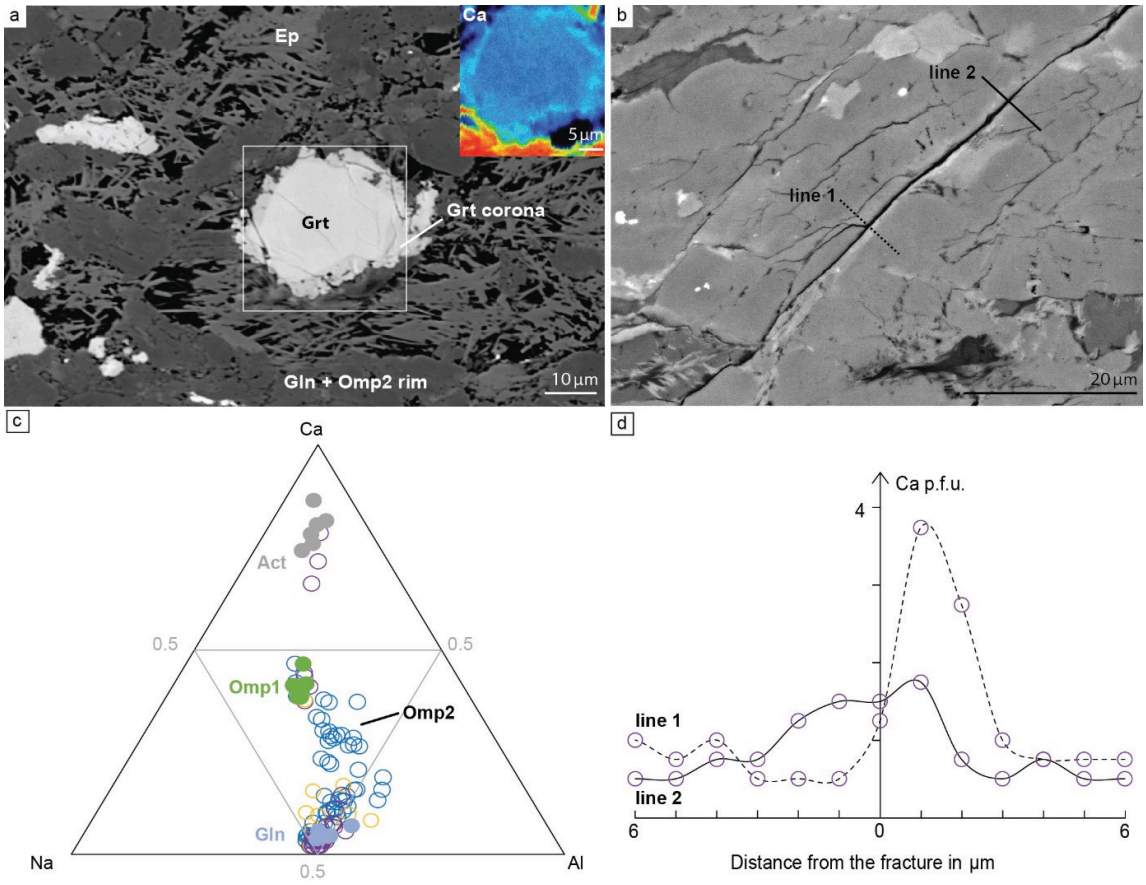

673

674 **Figure 6**: a) BSE image showing a brighter Grt core and a darker newly grown Grt corona.
675 The white rectangle marks the position selected for an element distribution map, which is
676 shown for Ca in the upper right corner. b) BSE image with the position of two line
677 measurements, which correspond to the two profiles in the Ca p.f.u. over distance plot in d).
678 c) Ca-Na-Al (a.p.f.u.) ternary plot for individual mineral compositions. Solid circles represent
679 WDX analysis of Act (grey), Omp1 (green), and Gln (purple) from the natural Corsican
680 blueschist. The open circles represent all WDX and EDX analyses on the deformed samples
681 (blue: bulk-rock, violet: Gln –rich, yellow: Lws –rich). d) Two profiles corresponding to the two
682 lines in b) showing Ca enrichment of the region on the fracture's wall.

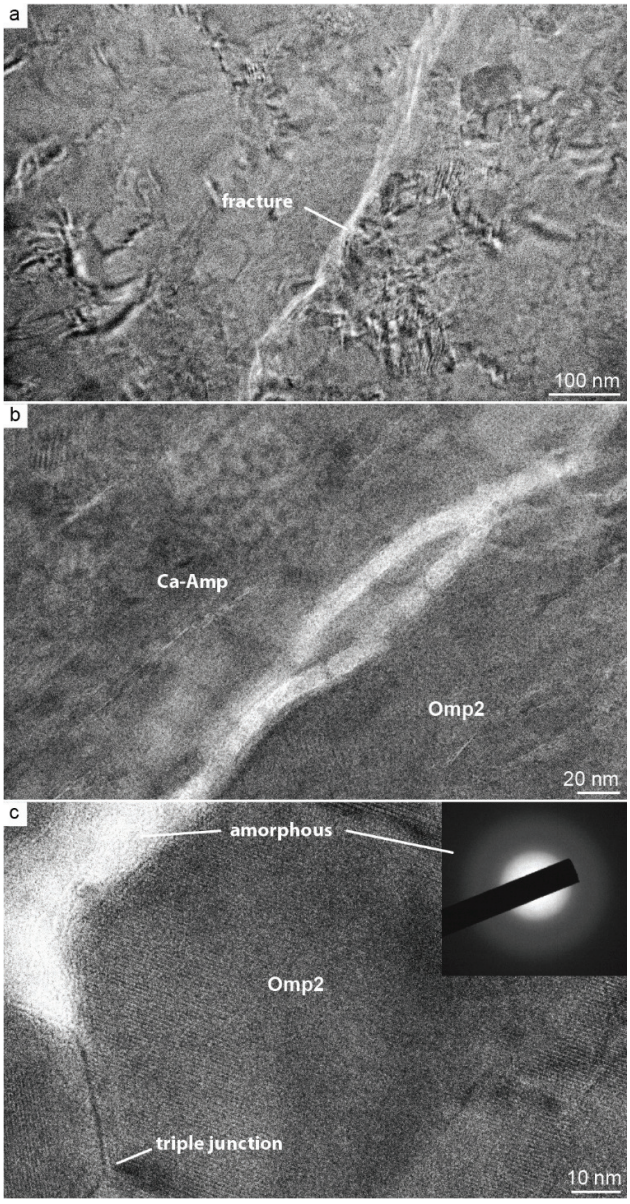

683

684 **Figure 7:** TEM images (BF mode) of the experiment GLN_2.5_927. a) The fracture appears
685 brighter. b) Closer zoom onto the fracture. On the upper left side of the fracture a Ca-Amp was
686 found, which shows a chemical composition close to actinolite. On the lower right side of the
687 fracture Omp2 was detected. c) Triple junction between three grains identified as Omp2. The
688 diffraction image in the upper right corner demonstrates that the material filling out the fracture
689 is amorphous.

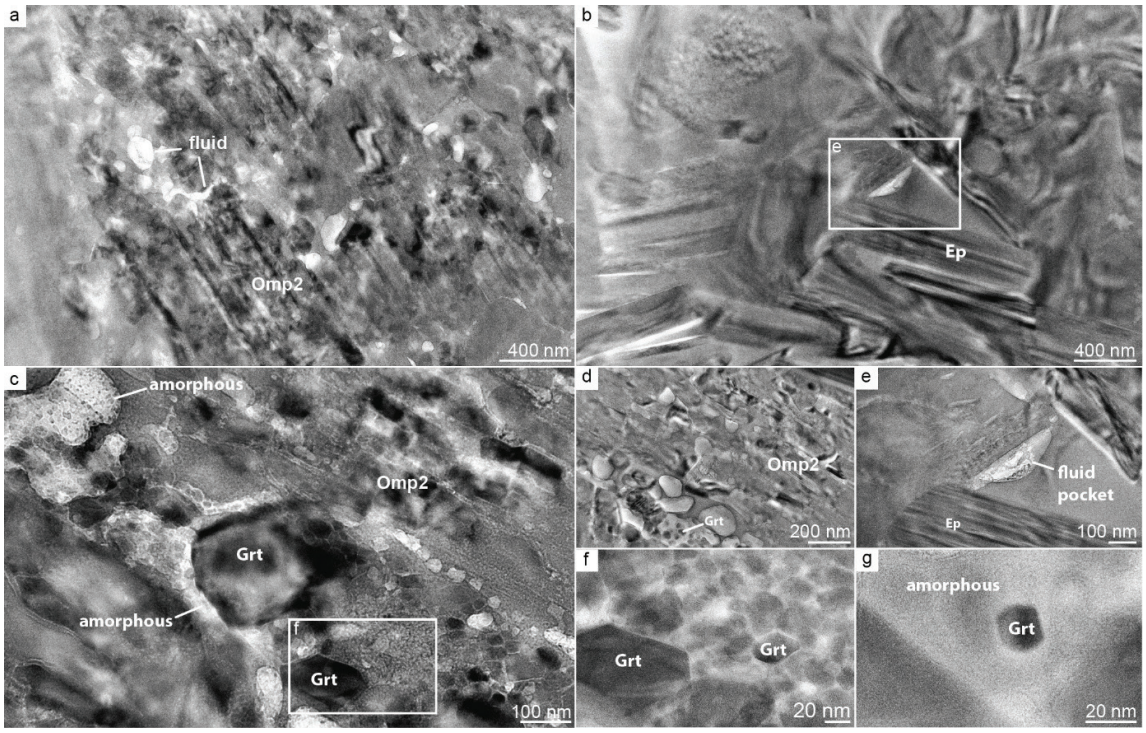

690

691 **Figure 8:** TEM images (BF mode) showing the nanostructure of the sample BS_3_1073. a)
692 Omp2 crystal surrounded by fluid. b) Epidote needles, the dehydration product of Lws, trapping
693 a fluid. The white rectangle shows the position of image e. c) Zoom onto the shear fracture
694 across which the FIB section was cut. The fracture appears brighter and shows many
695 idiomorphic Grt crystals “floating” within an amorphous material. In the upper right corner just
696 next to the fracture, small idiomorphic crystals appear which were identified as Omp2. The
697 white rectangle marks the position of the zoom shown in f. d) Closer zoom of an Omp2 crystal.
698 In the lower left corner of this image a brighter bubble-like structure appears, which
699 incorporates darker small crystals. The bright material is amorphous and the tiny crystals are
700 garnets. e) Zoom of the fluid pocket of image b. f) Closer zoom of the area marked with the
701 white rectangle in c. A brighter material surrounds idiomorphic garnet crystals. A mixture of
702 this bright, amorphous material and this idiomorphic Grt grains fills out the whole shear
703 fracture. g) Zoom of an idiomorphic Grt crystal “floating” within amorphous material.

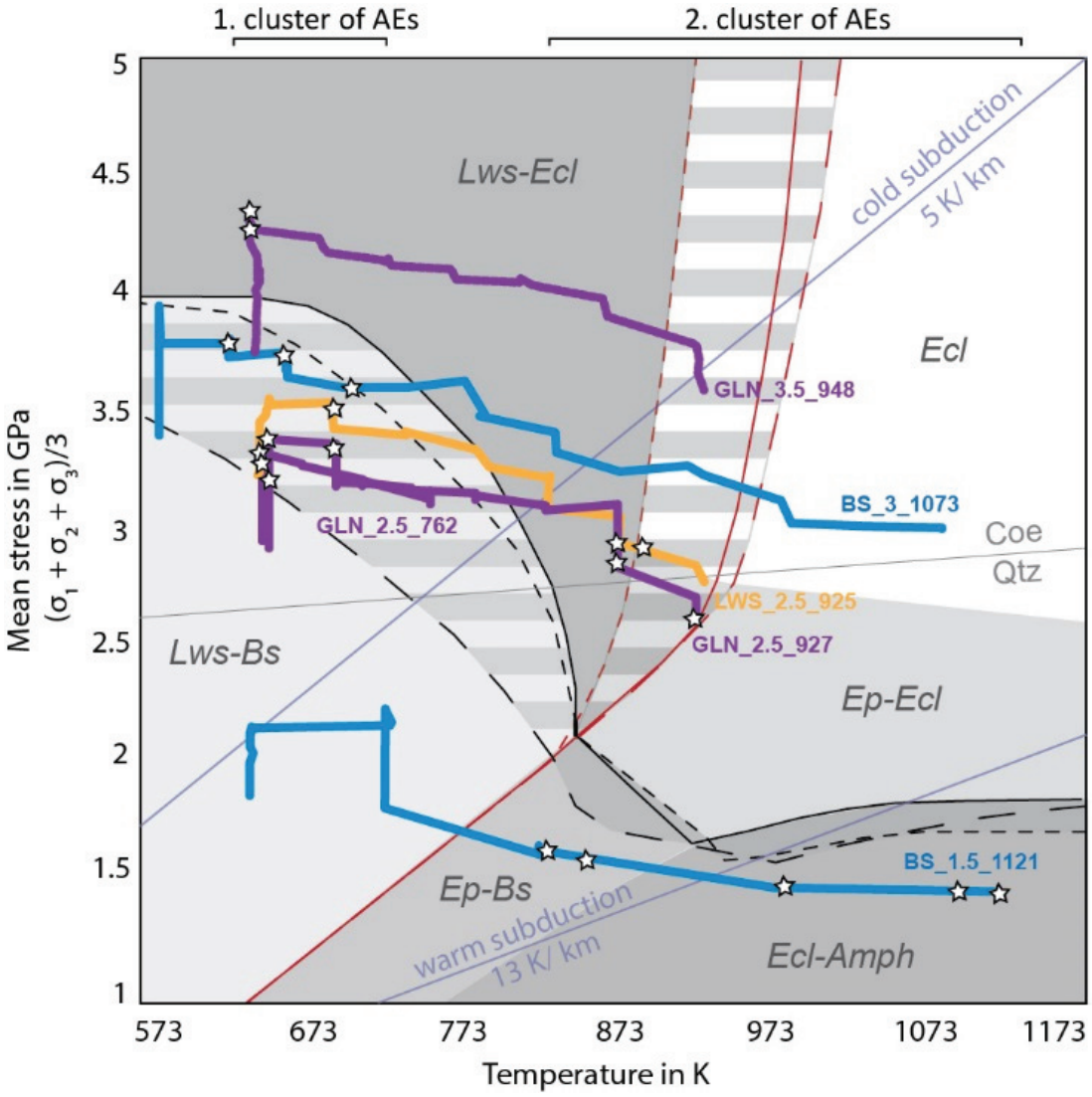

704

705 **Figure 9:** Mean stress versus temperature paths of all experiments superimposed to the same
706 *P-T* pseudosection as in **Figure 2**. Acoustic emissions recorded during the deformation are
707 represented as stars and often correlate with stress drops in the experimental mean stress
708 versus T curves. Most of the low-temperature AEs occurred prior to stress drops. The high-
709 temperature AEs were often recorded while heating and are not accompanied by bigger stress
710 drops. Two clusters of AEs are observed – the first at low-temperature, and the second at high-
711 temperature. The Amp- and the Lws-out reactions are indicated as in **Figure 2**. The low-
712 temperature cluster of AEs plots within the transition area between Lws-Bs and Lws-Ecl. The
713 second high-temperature cluster of AEs correlates with the breakdown of Lws.

714

715 **Tables**

716 **Table 1: Experimental conditions of the six D-DIA experiments.**

Sample	Experiment #	Starting material	P_c [GPa]	T range [K]	Strain rate [s^{-1}]	Maximum strain [%]
BS_3_1073	D1616	Bulk	3	583 - 1073	$4 \cdot 10^{-5}$	40
BS_1.5_1121	D1661	Bulk	1.5	649 - 1121	$7 \cdot 10^{-5}$	42
GLN_3.5_948	D1655	Gln-rich	3.5	659 - 948	$1 \cdot 10^{-5}$	42
GLN_2.5_927	D1618	Gln-rich	2.5	654 - 927	$2 \cdot 10^{-5}$	43
GLN_2.5_762	D1807	Gln-rich	2.5	656 - 762	$4 \cdot 10^{-5}$	37
LWS_2.5_925	D1667	Lws-rich	2.5	656- 925	$3 \cdot 10^{-5}$	40

717

718